#119

Fig. 5 Computer-processed image of the raw data presented in Fig. 2*b*. The Wiener filtering decreased the noise without affecting the periodic data.

These are the first images of amino acids to come from the emerging STM/AFM technology, and they reflect early progress in our effort to explore the fine structure of biological materials. Despite some promising results[14-18], it is still too soon to say how useful the scanning tunnelling microscope will be to the understanding of biological structure, mainly because the STM relies on electrical conductivity of the specimen to provide information. Biomolecules, for the most part, are not good conductors. The AFM, however, operates independently of specimen conductivity and may be better suited in the long run as a tool for studying atomic and molecular architecture of biological interest.

Although it has been useful for this initial research to obtain images from a periodic structure, it should be emphasized that periodic structures are not necessary for the atomic force microscope. In this respect the atomic force microscope is similar to a scanning tunnelling microscope. Many examples of isolated atomic scale features and point defects in periodic structures have been reported for the scanning tunnelling microscope[19]. It thus appears possible, at least in principle, to image molecules of biological importance that cannot be crystallized.

We thank W. Stoeckenius for emphasizing the opportunities for imaging proteins with the atomic force microscope, and I. Giaever for suggesting that amino acid crystals would be a good place to begin. We thank G. Binnig, Ch. Gerber, C. Quate, T. Albrecht, K. Wickramasinghe, R. Erlandsson, G. McClelland, C. Mate and S. Chiang for sharing advice on how to build atomic force microscopes and sending us preprints of their work; L. Dubois and M. Van Hove for information about surface reconstructions; S. Bartnicki-Garcia for providing the DL-leucine crystals; E. Martzen for secretarial help and M. Wilson and R. Stuber for help in the design and construction of our microscopes. This work was supported in part by the Belgian National Fund for Scientific Research (L.H.), the Agricultural Experiment Station, Purdue University Journal Paper No. 11, 597 (C.E.B.), Office of Naval Research (O.M., B.D.), and the National Science Foundation (S.G., P.K.H.).

Received 8 February; accepted 25 February 1988.

1. Binnig, G., Quate, C. F. & Gerber, Ch. *Phys. Rev. Lett.* **56**, 930-933 (1986).
2. Binnig, G., Gerber, Ch., Stoll, E., Albrecht, T. R. & Quate, C. F. *Europhys. Lett.* **3**, 1281-1286 (1987).
3. Marti, O., Drake, B. & Hansma, P. K. *Appl. Phys. Lett.* **51**, 484-486 (1987).
4. Mate, C. M., McClelland, G. M., Erlandsson, R. & Chiang, S. *Phys. Rev. Lett.* **59**, 1942-1945 (1987).
5. Albrecht, T. R. & Quate, C. F. *J. appl. Phys.* **62**, 2599-2602 (1987).
6. Marti, O., Drake, B., Gould, S. & Hansma, P. K. *J. Vac. Sci. Technol.* (in the press).
7. Marti, O. *et al. Science* **239**, 50-52 (1988).
8. Martin, Y., Williams, C. C. & Wickramasinghe, H. K. *J. Appl. Phys.* **61**, 4723-4729 (1987).
9. Martin, Y., Williams, C. C. & Wickramasinghe, H. K. *Appl. Phys. Lett.* **50**, 1455-1457 (1987).
10. Binnig, G. & Rohrer, H. *Rev. Mod. Phys.* **59**, 615-625 (1987).
11. *Crystal Data: Organic Compounds 1975-1978* 3rd edn Vol 5 (eds Donnay, J. D. H. & Ondik, H. M.) (National Bureau of Standards, Washington), 1983.
12. di Blasio, B., Pedone, C. & Sirigu, A. *Acta Crystallogr.* **B131**, 601; 2941 (1975).
13. Stoll, E. & Marti, O. *Surf. Sci.* **181**, 222-229 (1987).
14. Smith, D. P. E. *et al. Proc. natn. Acad. Sci.* **84**, 969-972 (1987).
15. Travaglini, G., Rohrer, H., Amrein, M. & Gross, H. *Surf. Sci.* **181**, 380-390 (1987).
16. Baro, A. M. *et al. Nature* **315**, 253-254 (1985).
17. Zasadinski, J. A. N., Schneir, J., Gurley, J., Elings, V. & Hansma, P. K. *Science* **239**, 1013-1015 (1988).
18. Lindsay, S. M. & Barris, B. *J. Vac. Sci. Technol. A* (in the press).
19. Slough, C. G., McNairy, W. W., Coleman, R V., Drake, B. & Hansma, P. K. *Phys. Rev. B* **34**, 994-1005 (1986).

Crystallography, chemistry and structural disorder in the new high-T_c Bi–Ca–Sr–Cu–O superconductor

D. R. Veblen*, P. J. Heaney*, R. J. Angel†, L. W. Finger†, R. M. Hazen†, C. T. Prewitt†, N. L. Ross†, C. W. Chu‡, P. H. Hor‡ & R. L. Meng‡

* Department of Earth and Planetary Sciences, The Johns Hopkins University, Baltimore, Maryland 21218, USA
† Geophysical Laboratory, Carnegie Institution of Washington, Washington, DC 20008-3898, USA
‡ Department of Physics, Texas Center for Superconductivity and Space Vacuum Epitaxy Center, University of Houston, Houston, Texas 77004, USA

High-temperature superconductivity with onset temperatures up to ~120 K has been observed recently in the Bi–Ca–Sr–Cu–O system[1,2]. The primary high-temperature superconducting phase has been identified by Hazen *et al.*[2] as a layer structure, probably related to the 22-K superconducting phase recently described by Michel *et al.*[3] and to the family of layered bismuth compounds described by Aurivillius[4]. Hazen *et al.* described the unit cell, approximate composition, and electrical properties of the Bi–Ca–Sr–Cu–O superconducting phase. Diffraction experiments indicate that the new Bi–Ca–Sr–Cu–O layer-structure superconductor possesses a primitive orthorhombic unit cell with probable space group *Pnnn*. The material exhibits severe structural disorder, which is primarily related to stacking within the layers. The apparent orthorhombic strucure is an average resulting from orthorhombic material mixed with monoclinic domains in two twinned orientations. We also describe two distinct types of structural disorder that are common in materials synthesized to date. This disorder complicates the crystallographic analysis and suggests that X-ray and neutron diffraction methods may yield only an average structure.

The present observations are from samples BCSCO-a and BCSCO-b of Hazen *et al.*[2]. All selected-area electron diffraction microscopy (SAED), X-ray analytical electron microscopy (AEM), and high-resolution transmission electron microscopy (HRTEM) experiments were performed with a Philips 420 transmission electron microscope, as described in detail by Livi and Veblen[5]. Cliff and Lorimer[6] thin-film *k*-factors for Ca and Cu were determined as noted in ref. 5, and those for Sr and Bi were determined from celestite (natural $SrSO_4$) and synthetic $BiVO_4$, combined with previously determined *k*-factors. The analyses are not highly accurate but they are clearly from single-crystal

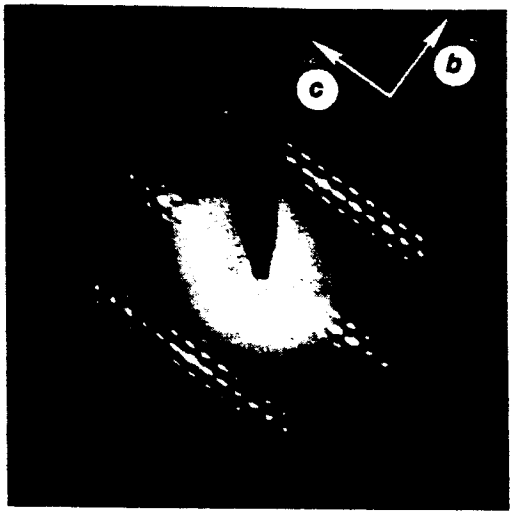

Fig. 1 An *a*-axis SAED pattern showing intense streaking parallel to c^*, due to severe structural disorder.

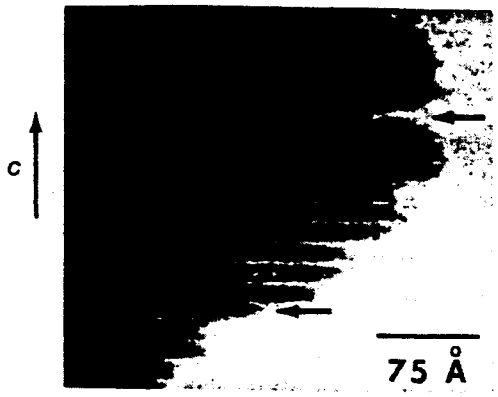

Fig. 2 Lattice image showing the 15.5-Å (002) fringes. Two defects involving missing or extra sublayers are arrowed.

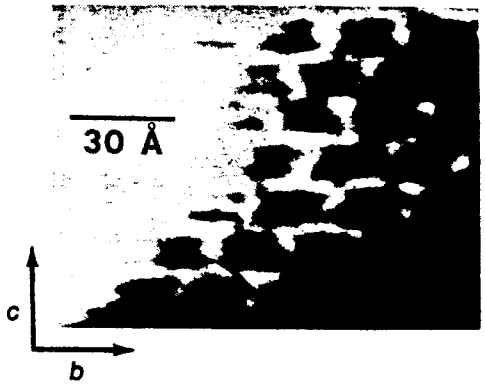

Fig. 3 Thin-crystal HRTEM image obtained parallel to *a* and labelled with the ideal orthorhombic unit cell axes. Light fringes paralel to (001) show the basic layer structure, while the light '010' fringes exhibit variable orientation as a result of stacking disorder.

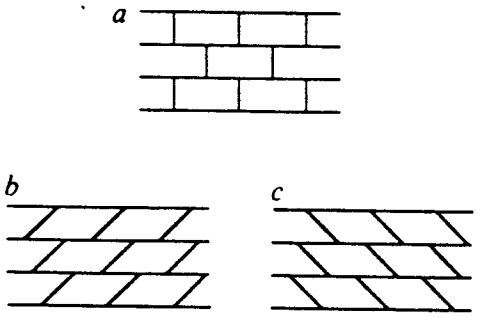

Fig. 4 Schematic diagram of the structure observed in lattice images from thin crystals; *a*, ideal orthorhombic structure with vertical '010' fringes; *b*, and *c*, the two twin orientations of the monoclinic domains with tilted '010' fringes, which combine to form an average orthorhombic structure in electron and X-ray diffraction patterns.

material of the superconducting phase and not from a mixture. The quality of the lattice images is rather low, because the layered crystals are quite thick in orientations with the electron beam parallel to the layers and because most crystals are deformed and hence do not represent a unique crystallographic orientation. They are, however, of sufficient quality to allow determination of the large-scale defect structures.

SAED patterns obtained parallel to the *a* and *c* crystallographic axes suggest[2] an orthorhombic unit cell. This identification was refined using powder X-ray diffraction data. The unit cell has parameters $a = 5.41$, $b = 27.2$, $c = 30.8$ Å, which may be related to a cubic perovskite subcell by the ratios $\sqrt{2} \times 5\sqrt{2} \times \sim 8$. Based on the systematic absence of diffraction spots with $h = 0$, $k + l = 2n + 1$, on *a*-axis SAED patterns, Hazen *et al.*[2] suggested that the oxide might possess an *A*-centred unit cell.

We have now obtained both SAED patterns and HRTEM lattice images parallel to all three crystallographic axes as well as other orientations. These patterns confirm that the unit cell is orthogonal, with all three unit cell angles $\alpha = \beta = \gamma = 90°$, consistent with orthorhombic lattice geomtry. Intensity distributions also are consistent with the orthorhombic crystal system.

In addition to the systematic absence noted above, *b*-axis SAED patterns show that diffraction spots with $k = 0$, $h + l = 2n + 1$, are absent, consistent with a body-centred (*I*-centred) lattice or *n*-glide planes parallel to (010). The *a*- and *b*-axis SAED patterns indicate that most apparent violations of *I*-centring visible on the *c*-axis patterns result from the intersection with the Ewald sphere of relatively strong streaks that are present in all diffraction rows parallel to c^*, as a result of structural disorder. The intensities of the strongest apparent violations (the 100, 090, and 0·11·0 spots in Fig. 3 of Hazen *et al.*[2]) are probably enhanced by dynamical diffracton, due to their relationships to the strong perovskite subcell diffractions.

The electron diffraction extinctions noted above contain clear violations of face centring, as well as all possible orthorhombic end-centred lattices (*F*, *A*, *B* and *C*), and these violations cannot be accounted for by dynamical diffraction. In addition, diffractions such as the 15*l* with $l = 2n + 1$ are present, in violation of body-centring. The lattice thus appears to be primitive (*P*). The observed space group extinctions indicate *n*-glide planes normal to *c*, *b* and probably *a*, suggesting space group *Pnnn*, or possibly *Pnn2* or *Pnnm*. It should further be noted that entire classes of reflections, such as the 15*l*s with $l = 2n$ are absent. These non-space-group extinctions probably imply that the structure possesses some sort of strong pseudosymmetry or local symmetry.

It must be emphasized that the unit cell and space-group symmetry under discussion refer only to the average structure of this superconducting oxide. It is clear from data presented below that the true structure consists of small domains probably having both monoclinic and orthorhombic symmetries.

AEM data from thin, single-crystal plates of the oxide show that the material is chemically rather homogeneous. As the AEM

analyses are from indisputably single-phase material that exhibited SAED patterns characteristic of the superconductor, these data support the assumption that the superconductor possesses a unique structural formula, although compositional variations among synthesis runs can be expected to occur due to solid solution. The AEM data show rough consistency with the data of Hazen *et al.*[2], although the latter used experimental techniques with much lower spatial resolution. When normalized to 7.00 cations, for comparison with the data of Hazen *et al.*, the analyses yield the formula

$$(Bi_{1.80}Cu_{2.20})_{\Sigma 4.00}(Ca_{1.25}Sr_{1.73}Bi_{0.02})_{\Sigma 3.00}O_{8+\delta}$$

Determination of the full crystal structure is necessary for full understanding of the chemical substitutions within this formula.

SAED patterns of the oxide show reasonable periodicity parallel to a^* and b^* but tend to be heavily streaked parallel to c^* (Fig. 1), indicative of structural disorder affecting the d_{00l} periodicity. Lattice images confirm that the structure is highly periodic within the a-b plane, but at least two different types of disorder are readily observed in HRTEM lattice images obtained by imaging diffraction patterns containing c^*. One-dimensional lattice images produced from only the $00l$ row of diffraction spots show occasional layers with contast or spacing different from that of the bulk structure (Fig. 2; also see Fig. 4 in ref. 2). Assuming that the oxide is related to the perovskite structure, these defects are probably due to missing and extra perovskite sublayers, perhaps accompanied by anomalous cation occupancies. The most common defects of this sort appear to involve a single missing or extra unit of ~4 Å thickness parallel to the c-axis.

Another type of disorder, observed in images obtained with the electron beam parallel to a, appears to be pervasive and probably results in most of the streaking parallel to c^* in SAED patterns. These a-axis images (Fig. 3) show relatively light fringes that are rigorously parallel to (001) and another set of light fringes that are more or less parallel to (010), hereafter referred to as the '010' fringes. Although the average crystal structure of this oxide has not yet been determined, it is likely that these light (001) and '010' fringes correspond to two different sets of planes with relatively low electron and proton density.

Although the '010' fringes in lattice images are in places parallel to (010) of the orthorhombic unit cell, they commonly deviate from this orientation in either of the two possible senses, forming variable angles other than 90° with the (001) fringes. This is shown schematically in Fig. 4. The structures of Fig. 4*b* and *c* correspond to monoclinic domains related to each other by a (010) mirror twin operation. The true structure of this material may thus be a mixture of an orthohombic structure (Fig. 4*a*) with twinned monoclinic structure (Fig. 4*b* and *c*), exhibiting variable angles between the (001) and (010) planes. Microtwinning of such monoclinic domains is shown in Fig. 5*a*. In addition, the mixing of these orthorhombic and monoclinic domains results in orientation variations in the 011 fringes on lattice images (Fig. 5*b*).

Although there is no direct diffraction data relating to the space group of the monoclinic structures, it is likely that it is a distortional subgroup of the ideal orthorhombic space group *Pnnn*. Assuming that the n-glide normal to a is preserved, the space group is probably $P2/n$, having a non-conventional monoclinic unit cell with a unique.

A final defect that is observed in a-axis lattice images can be described as a dislocation in the superstructure with apparent projected Burgers vector $\frac{1}{2}[011]$. An example is illustrated in Fig. 5*c*. This type of defect can be accommodated by adjusting the stacking of (001) layers in the region of the fault.

We have clarified the crystallography of the new high-T_c Bi-Ca-Sr-Cu-O layered superconductor, showing that its average structure is probably best described with a primitive orthorhombic unit cell, with space group *Pnnn*. However, our lattice imaging experiments also show that the material grown to date possesses pervasive structural disorder. The structure has occasional missing and extra sublayers. More important, we have shown that the average orthorhombic structure actually consists of a complex mixture of orthorhombic material with monoclinic material (probable space group $P2/n$) in two twinned orientations and having variable angles between the (001) and '010' fringes. The variable angles may result from variations in the stacking of rows of low metal occupancy or atomic number

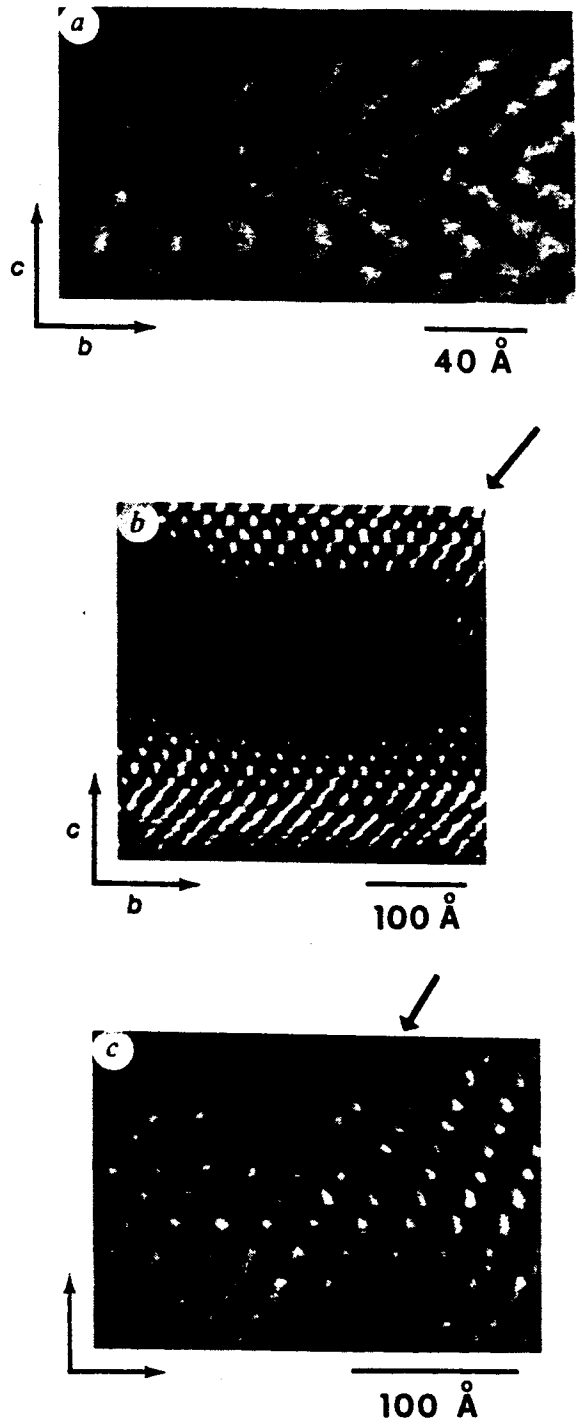

Fig. 5 Lattice images showing (011) fringes. Axes refer to ideal orthorhombic structure. The chevron structure in (*a*) is due to small-scale twinning of two monoclinic structures. Varying orientation of the fringes in (*b*), due to stacking disorder, and the dislocation in the superstructure in (*c*), with apparent projected Burgers vector $\frac{1}{2}[011]$, are best seen by viewing the images a low angle in the direction of the arrows.

in adjacent sublayers. It is also possible that the twinned monoclinic structure results from a phase transition from a higher-temperature orthorhombic structure.

We speculate that two different types of layers corresponding to the light (001) and '010' fringes may be responsible for the two components of superconductivity. The component with onset temperture ~120 K may result from local superconductivity within the '010' layers, while the lower-temperature component may result from superconductivity in the (001) layers. It is thus possible that this structure represents a three-dimensional superconductor.

This work was supported by NSF, NASA, the Texas Center for Superconductivity and the TLL Temple Foundation (Houston). We are indebted to Dr J. E. Post of the Smithsonian Institution for AEM analytical standards.

Received 11 February; accepted 3 March 1988.

1. Chu, C. W. *et al. Phys. Rev. Lett.* **60**, 941–943 (1988).
2. Hazen, R. M. *et al. Phys. Rev. Lett.* **60**, 1174–1177 (1988).
3. Michel, C. *et al. Z. Phys.* (submitted).
4. Aurivillius, B. *Arkiv Kemi* **1**, 463–480; 499–512 (1949); **2**, 519–527 (1950).
5. Livi, K. J. T. & Veblen, D. R. *Am. Miner.* **72**, 113–125 (1987).
6. Cliff, G. & Lorimer, G. W. *J. Microscopy* **103**, 203–207 (1975).

The mechanism of operation of tin(IV) oxide carbon monoxide sensors

P. G. Harrison* & M. J. Willett†

* Department of Chemistry, University of Nottingham, University Park, Nottingham NG7 2RD, UK
† British Coal Corporation, HQ Technical Department, Ashby Road, Bretby, Staffordshire DE15 0QD, UK

The electrical properties of tin(IV) oxide render it an excellent material for the detection of very low levels of carbon monoxide, and several devices based on sintered pellets of SnO_2 are commercially available[1,2]. Investigations of the operation of such sensors have generally been restricted to studies of the electrical behaviour of the oxide and little attention has been paid to the relationship between the surface adsorption phenomena and electrical changes in the bulk oxide. These studies[3] demonstrated the consistency of a model in which conductance is effectively controlled by the population of negatively charged oxygen adsorbates. The chemical reactions occurring at the oxide surface, although unsubstantiated, have been assumed to involve CO adsorption, desorption of CO_2 (which produces an increase in conductance) and replenishment of the resulting surface oxygen vacancy by adsorption of molecular oxygen[4]. Here we describe experiments in which the nature of the surface species adsorbed into tin(IV) oxide from atmospheres containing low levels of carbon monoxide is monitored using transmission infrared spectroscopy while simultaneously measuring the electrical changes produced in the bulk oxide. The data demonstrate the effect of heat treatment on the formation of adsorbate species and the mutual interdependence of adsorbate species and bulk oxide electrical conductance. This relationship is important both for sensor operation and heterogeneous catalysis.

The tin(IV) oxide sample used for each experiment comprised a thin self-supporting pressed disk of high-surface-area gel (prepared by the hydrolysis of tin(IV) chloride). Two electrodes attached to the disk surface using gold paste allowed the electrical conductance to be continuously monitored. The sample was mounted in a twin-beam infrared cell provided with an integral furnace, which was positioned in the optical path of a dispersive infrared spectrometer and connected to a high vacuum system. Using this arrangement the oxide disk could be preheated at a temperature up to 660 K, exposed to atmospheres of any desired composition or pressure (usually 10^5 Pa), and the gas phase could be removed rapidly by evacuation. All the data reported here were obtained with the oxide sample held at 329 K.

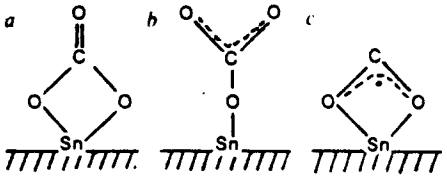

Fig. 1 Structures of the surface species formed on tin(IV) oxide from CO/air mixtures. *a*, Bidentate carbonate (characteristic infrared bands; 1,585, 1,223 cm^{-1}). Unidentate carbonate (1,430, 1,370 cm^{-1}). *c*, Carboxylate (1,540, 1,300 cm^{-1}).

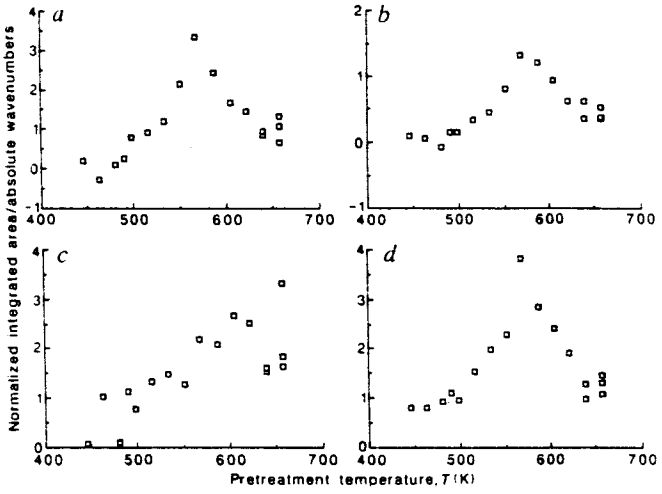

Fig. 2 Plots of the integrated peak areas against oxide pre-treatment temperature for the bands at 1,585 cm^{-1} (*a*), 1,223 cm^{-1} (*b*), 1,300 cm^{-1} (*c*), and 1,430 cm^{-1} (*d*).

Infrared difference spectra due to surface adsorbed species were obtained by subtracting the oxide absorptions from those observed in the oxide plus absorbate system. The spectra observed on dosing the tin(IV) oxide disk with 1,000 p.p.m. CO in dry air comprise five major bands corresponding to three types of surface species: surface unidentate and bidentate carbonate, and a surface carboxylate (Fig. 1). The intensities of all the bands due to the adsorbate species increase steadily with time during the period of exposure. Removal of the CO/air atmosphere by evacuation followed by re-exposure to dry air produces no new infrared features but the bands due to surface unidentate and bidentate carbonate are greatly reduced in intensity. In contrast, those due to surface carboxylate are only slightly affected. It would appear that whereas both the surface carbonate species are readily desorbed, the surface carboxylate species are held more strongly.

The pre-treatment temperature of the oxide has a marked effect on the abundances of the three types of surface species formed. The absorption intensities (and hence the surface population) of both of the surface carbonate features increase with increasing calcination temperature up to ~570 K and decline rapidly thereafter. The absorption peaks for carboxylate, however, increase fairly steadily up to at least 620 K. These effects are clearly demonstrated by evaluating integrated peak areas for the characteristic peaks of each species, and in Fig. 2 these are plotted against oxide calcination temperature for the 1,223 cm^{-1}, 1,585 cm^{-1} (both due to bidentate carbonate), 1430 cm^{-1} (unidentate carbonate), and 1,300 cm^{-1} (carboxylate) features respectively. Clearly the nature of the adsorbed species formed from CO/air atmospheres varies significantly depending upon the conditions, and at higher pre-treatment temperatures